www.sciencemag.org/content/355/6324/494/suppl/DC1

# Supplementary Materials for

## Imaging rotational dynamics of nanoparticles in liquid by 4D electron microscopy

Xuewen Fu, Bin Chen, Jau Tang,* Mohammed Th. Hassan, Ahmed H. Zewail

*Corresponding author. Email: jautang@caltech.edu

Published 3 February 2017, *Science* **355**, 494 (2017)
DOI: 10.1126/science.aah3582

**This PDF file includes:**



**Other Supplementary Material for this manuscript includes the following:**
(available at www.sciencemag.org/content/355/6324/494/suppl/DC1)

## Materials and Methods

Preparation of liquid cell sample

The liquid cell contains a thin layer of solution sandwiched between two electron-transparent silicon nitride ($Si_3N_4$) membranes at the visualization window. The details of the liquid cell fabrication have been widely described in previous publications (*6, 7*). In the present work, we have used a similar but simplified protocol with some modifications. Standard transmission electron microscope (TEM) $Si_3N_4$ windows (250 μm × 250 μm) on a 200-μm-thick silicon frame (circular shape that fits the standard TEM holder) with a thin layer of gold film (~200 nm) as a spacer were used (customized from Norcada Inc.), where the gold film spacer does not block the electron transparent window (Fig. 1B). The ultrathin low-stress $Si_3N_4$ membrane is approximate 20 nm thick, which is deposited by low-pressure chemical vapor deposition. This guarantees the spatial resolution of the liquid cell to be in nanometer range.

The preparation of liquid cells is given as follows. First, the $Si_3N_4$ window chips were rinsed with acetone, isopropyl alcohol, and deionized water followed by plasma cleaning ($P$ ~ 3.5 W) for 30 s. The plasma cleaning is extremely important as it makes the $Si_3N_4$ membrane hydrophilic to aqueous solution. After that, a drop of ~5 μL aqueous solution with citrate capped gold nanoparticles (NPs, purchased from Nanocomposix Inc.) was loaded on the bottom chip with spacer, and another top chip without spacer was put on the surface of the liquid (see Fig. S2). Due to the tension of the liquid, the top $Si_3N_4$ window would rotate freely and align well with that of the bottom one automatically. These two well-aligned $Si_3N_4$ window chips were clamped by a tweezer, and the superfluous liquid was then absorbed by a small piece of filter paper from the side. A thin layer liquid was therefore sandwiched between the two chips with a thickness nearly equivalent to the spacer thickness. Finally, an epoxy adhesive (Ted Pella Inc.) was used to seal the side of the liquid cell. When the sealing was dried, the liquid cell was loaded in our four-dimensional electron microscopy (4D-EM) for measurements. The gold NP-dimers studied in this work were formed in the NP population due to the aggregation or coalescence of NPs through the photothermal effect induced by femtosecond (fs) laser pulses illumination (520 nm wavelength, 350 fs duration, 1 kHz repetition rate, fluence of 2~4 mJ/cm$^2$).

During the experiment, we checked each liquid cell by tilting it to different view angles and excluded the bad one with gas bubbles or with apparent bulges. For the good liquid cell with a continuous liquid layer, there may exist a little bulge when put in the high vacuum of TEM, owing to the large area of the $Si_3N_4$ window of the liquid cell (250 × 250 μm$^2$). However, the observed NP-dimer rotation only occurs in a small area of <1×1 μm$^2$, the possible existence of a small bulge should not significantly influence the observed rotation dynamics of the NP-dimers in such a small area shown in our work.

**Supplementary Text**

Calculation of MSAD for the NP-dimer

For the analysis of the statistical properties of the rotation angle of a NP-dimer, we performed the widely used statistical method (*33*) to calculate its time-dependent mean square angular displacement (MSAD) based on Einstein's model. A set of snapshots at $t_0$, $t_1$, $t_3$, ……, and $t_N$ of the NP-dimer were extracted from the movie of its rotational dynamics with a time interval of $\Delta t$. The rotation angle of the NP-dimer at each time point relative to its initial orientation at $t_0$ can be determined as $\theta(t_0)$, $\theta(t_1)$, $\theta(t_3)$, ……, and $\theta(t_N)$, respectively. Then the MSAD at $t = \Delta t$ is given by

$$MSAD(t = \Delta t) = \frac{\sum_{k=1}^{N} [\theta(t_k) - \theta(t_{k-1})]^2}{N} \quad (1)$$

likewise, at $t = n\Delta t$

$$MSAD(t = n\Delta t) = \frac{\sum_{k=n}^{N} [\theta(t_k) - \theta(t_{k-n})]^2}{N - (n-1)} \quad (2)$$

where $n$ is a number from 0 to $N$. As $n$ approaches $N$, the number for data averaging becomes fewer and the statistics for MSAD becomes lower at longer times.

Numerical simulations of random rotation

We performed numerical simulations to explore the statistical properties of random rotation. Since the rotation only occurs in clockwise (negative) or counter-clockwise (positive) direction for the random rotation in a two-dimensional plane, and both the direction and the step length of the rotation are random, it is in fact a typical one-dimensional random walk problem. Therefore, we assumed a scheme of one-dimensional random walk for our rotational dynamics.

Because the experimentally retrieved exponent $\alpha$ of the MSAD for the NP-dimer rotation strongly depends on the bias of the angular displacement distribution which is dominated by the morphological asymmetry of the NPs (see the main text), we performed numerical simulations on the MSADs of three types of random rotation with different biased angular displacement distributions: [0.5, 0.5] (bias of 0), [0.75, 0.25] (bias of 0.5) and [1, 0] (bias of 1), where in [c1, c2] the values c1 and c2 represent the probability of clockwise and counter-clockwise rotation, respectively. In our numerical simulations, we used a random number generator to generate a random number between 0 and 1 to control the rotation direction of either counter-clockwise (positive) or clockwise (negative). The step length for the rotation, however, is controlled by another random number generator with a Gaussian weight. For the first case with an angular displacement distribution of [0.5, 0.5], the probability for either rotation direction is identical, which represents the conventional diffusive rotation. For the second case with a biased angular displacement distribution of [0.75, 0.25], the probability of the clockwise rotation is 0.75 and is higher than that (0.25) of the counter-clockwise rotation. For the third case with a totally biased angular displacement distribution of [1, 0], it signifies the unidirectional random rotation with only clockwise rotation but no counter-clockwise rotation.

The numerical simulation results are presented in Fig. S11. For the angular displacement distribution of the random rotation without bias ([0.5, 0.5]), the MSAD is proportional to the number of steps $N$ (corresponding to the time $t$ in the experiment), namely, $MSAD \propto N$, which is in accord with the well-known prediction of Einstein's theory of rotational Brownian motion, i.e. the conventional diffusive rotation. However, when the angular displacement distribution biases to one direction, such as [0.75, 0.25], the MSAD has a power dependence with the exponent $\alpha$>1, which deviates from the result of Einstein's model and shows a superdiffusive rotation. For the case of unidirectional random rotation with a totally biased displacement distribution ([1, 0]), $MSAD \propto N^2$, which displays a ballistic rotation.

Based on our numerical simulations and experimental results, for this verified full transition of the rotational dynamics, the MSADs follow a power-law form of $<[\Delta\theta(t)]^2>= C \cdot t^{\alpha}$, $(1 \le \alpha \le 2)$, where $C$ is a constant, and the exponent $\alpha$ depends on the bias of the angular displacement distribution. The case of $\alpha = 1$ describes the conventional diffusive rotation, where $C = 2D_r$ ($D_r$ is the rotational diffusion coefficient); $\alpha > 1$ corresponds to the superdiffusive rotation, and the extreme case of $\alpha = 2$ corresponds the ballistic rotation, where $C = \omega_{rms}^2$ ($\omega_{rms}$ is the rms angular velocity).

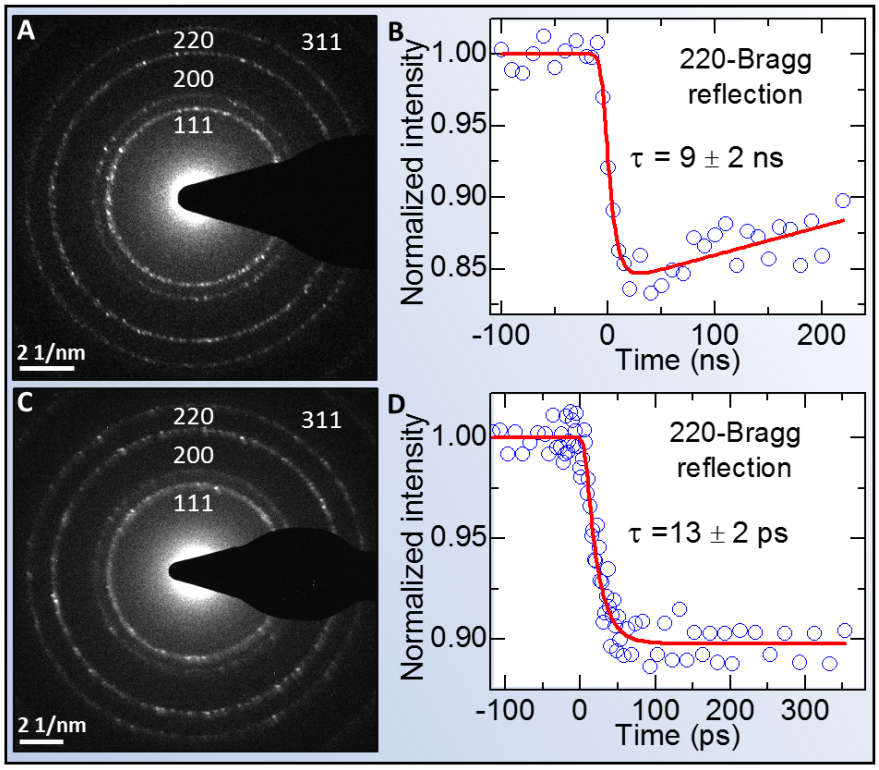


**Fig. S1. Calibration of the coincidence of the pump (fs) and the probe (fs or ns) pulses.** (**A** and **C**) Diffraction patterns of a poly-crystallized aluminum film obtained with ns- and fs-probe electron pulses, respectively. (**B** and **D**) The diffraction intensity change of the Bragg reflection (220) as a function of the delay time obtained by ns-pump (laser pulse)/ns-probe (electron pulse) and fs-pump (laser pulse) /fs-probe (electron pulse) configurations, respectively. The pump fluence of these two measurements was 5 mJ/cm$^2$. The time constants of 9 ± 2 ns and 13 ± 2 ps, respectively, were obtained from the exponential fit.

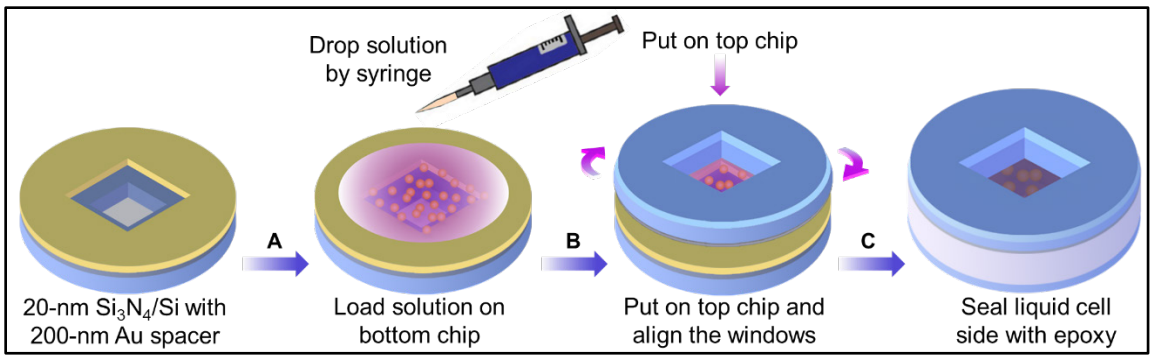


**Fig. S2. Protocol for liquid cell preparation.** (**A**) After $Si_3N_4$ window chips were rinsed with acetone, isopropyl alcohol, and deionized water and followed by plasma cleaning (*P* ~ 3.5 W) for 30 s, a drop of ~5 μL aqueous solution with the gold NPs was loaded on the bottom chip. (**B**) Another top chip without gold film spacer was put on the surface of the liquid, which would rotate freely and align well with that of the bottom one automatically due to the surface tension of the liquid. (**C**) These two well-aligned $Si_3N_4$ window chips were clamped by a tweezer and the superfluous liquid was absorbed by a small piece of filter paper from the side. Then an epoxy adhesive was quickly used to seal the side of the liquid cell by using a needle under an optical microscope.

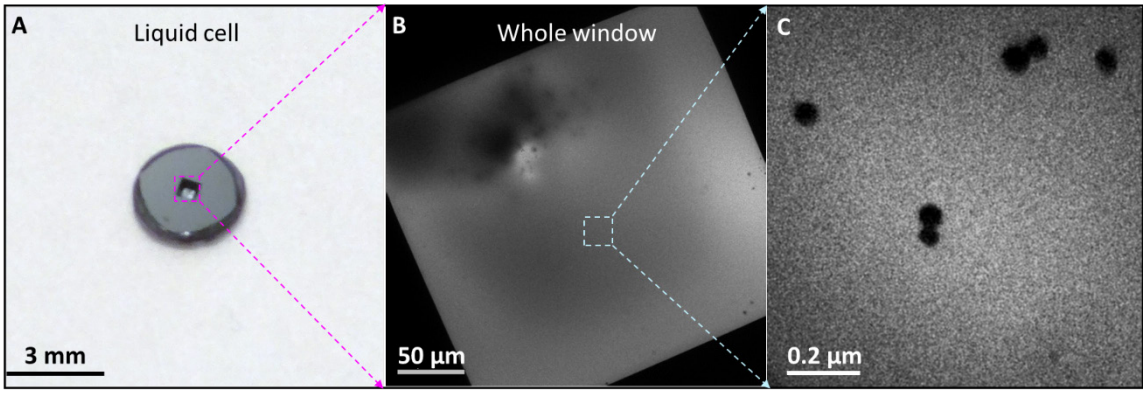


**Fig. S3. Photograph (A), overall micrograph of the whole window (B) and the zoom in image (C) of the liquid cell.**

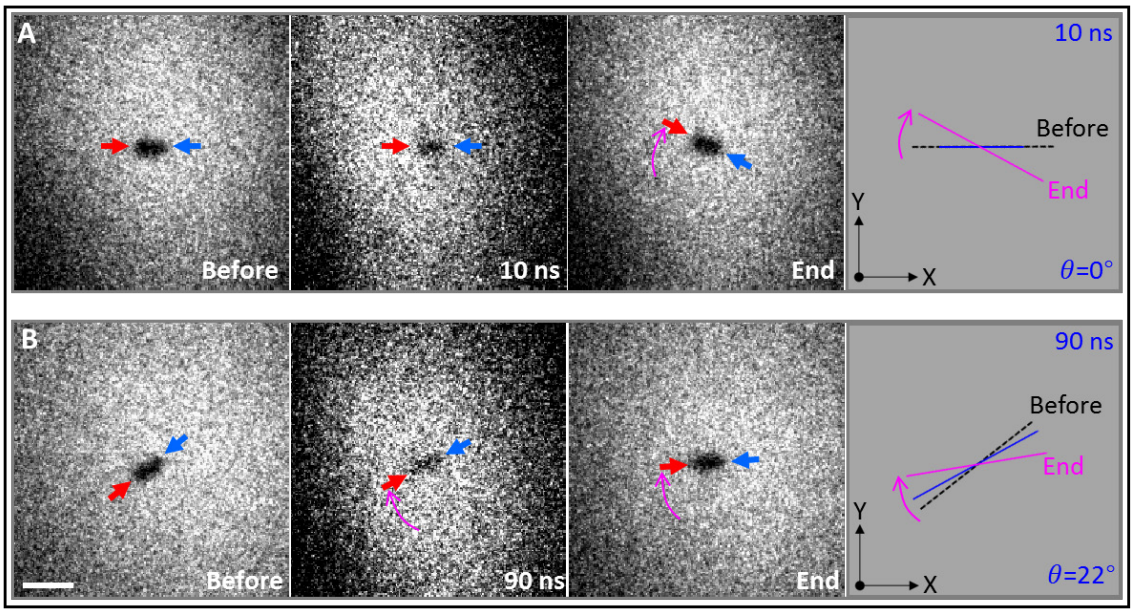


**Fig. S4. Magnitude of the rotation angle at early (10 ns) and later (90 ns) times. These two data points are shown in Fig. 3A (in the main text). The scale bar is 200 nm.**

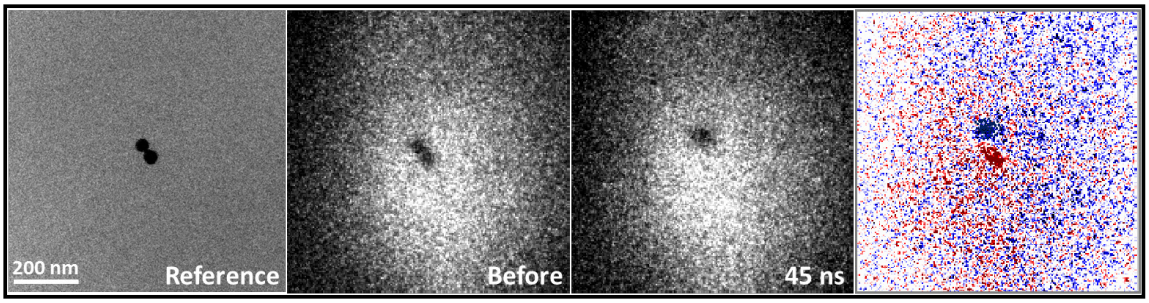


**Fig. S5. Single-shot imaging of NP-dimer fusion dynamics.** (First column) Continuous e-beam image of the initial NP-dimer shown as a reference (without laser excitation). (Second and third columns) Single-shot images of the NP-dimer before and at a delay of 45 ns after the pump pulse ($J$ = 48 mJ/cm$^2$, above the melting threshold of gold NPs), respectively. (Last column) The difference images obtained by subtracting the single-shot image before the pump pulse from that at the 45 ns delay. Negative and positive contrasts are indicated by blue and red, respectively.

Under the high laser fluence above the melting threshold, the NP-dimer fuses into a bigger spherical particle in 45 ns after the laser pulse. This result confirms the strong local photothermal effect. It demonstrates that the configuration of the NPs in aqueous solution can be efficiently controlled in situ by controlling the fluence, the time window and the sequence of ultrashort laser pulses.

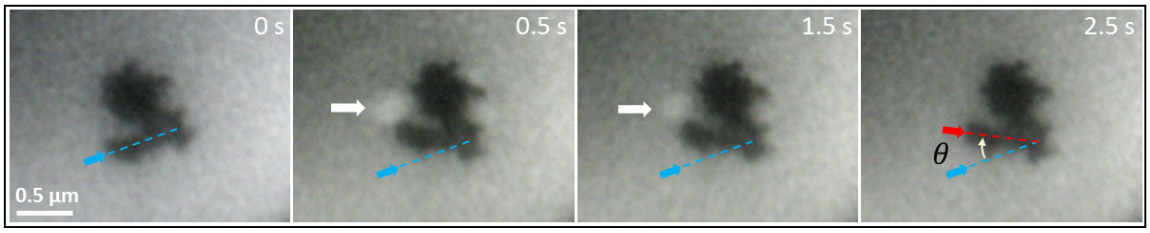


**Fig. S6. Rotation of a gold NP-cluster induced by a single fs-laser pulse (see also Movie S2).** (First column) Image of the gold NP-cluster before laser pulse excitation. (Second to fourth columns) Snapshots of the gold NP-cluster at different times after a single fs-pulse excitation (fluence 20 mJ/cm$^2$). The blue dash lines show the initial orientation of the NP-cluster, while the red dash line shows its final orientation after the single pulse excitation. The white arrows indicate the steam nanobubble (NB) induced by the fs-laser pulse heating of the gold NP-cluster, which actuates the rotation the NP-cluster. Because of the high laser fluence and the strong absorption of the NP-cluster and thus the huge photothermal effect, a big NB is generated near the NP-cluster. The rapid nucleation and expansion of the NB induce a force and torque on the NP-cluster and actuate the rotation. This rotation process is very fast as it is almost complete in the first snapshot (0.5 s). However, the NB takes 1~2 s to vanish due to its big size and the continuous heat dissipation from the hot NPs.

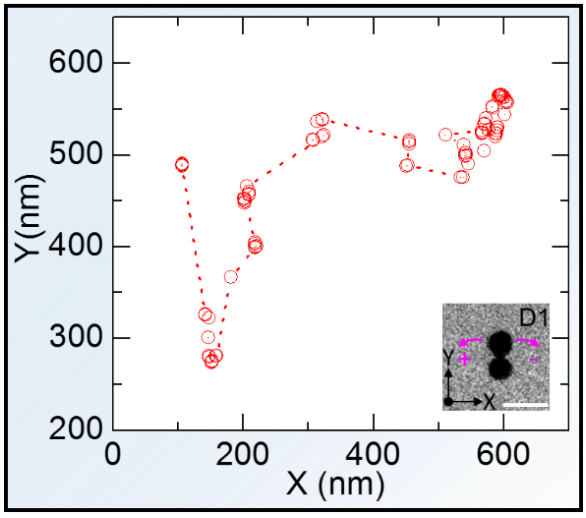


**Fig. S7. Trajectory of the center of mass of D1 dimer under fs-laser illumination (repetition rate 1kHz, fluence 2.4 mJ/cm$^2$) from 0 to 27 s (see also Movie S3). Scale bar is 100 nm.**

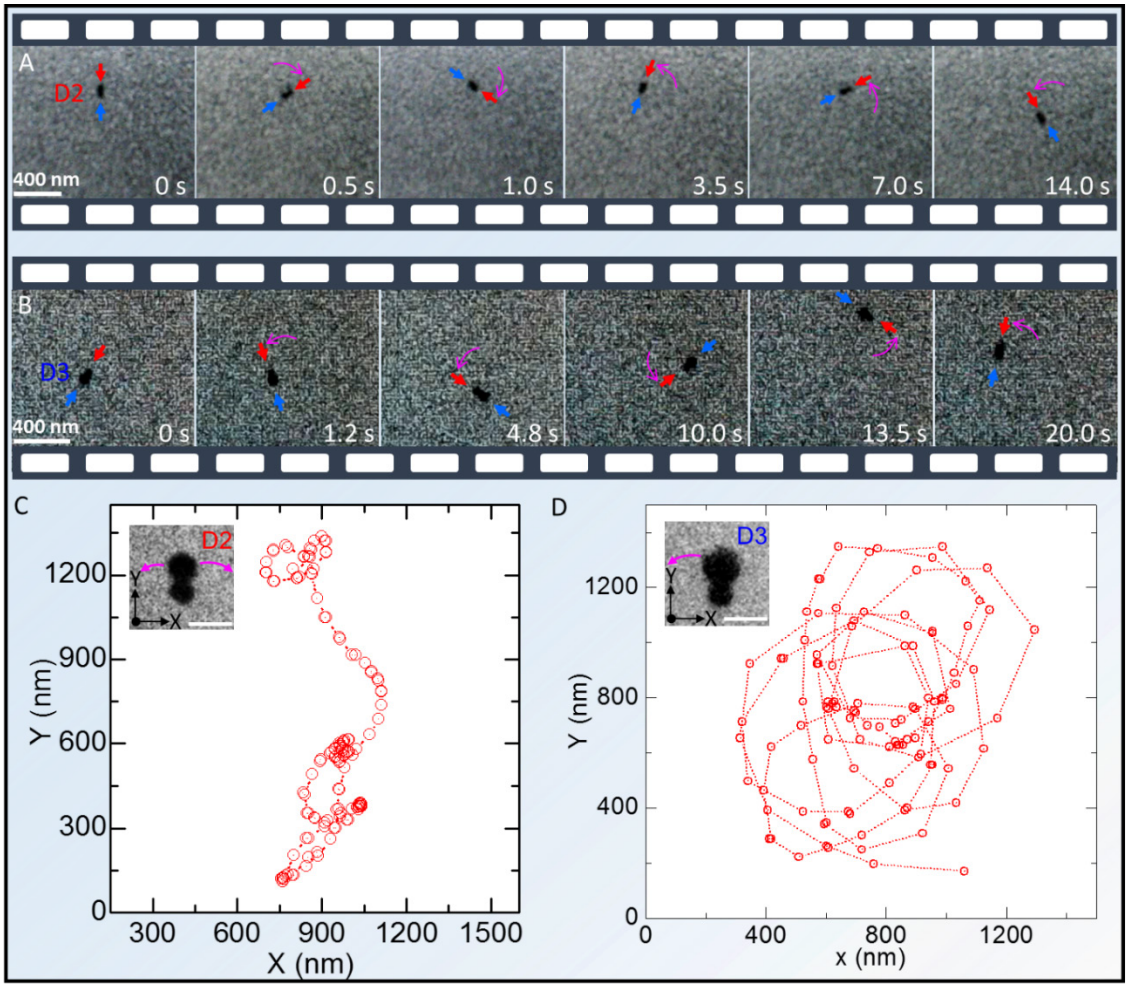


**Fig. S8. Trajectories of the center of mass of D2 and D3 dimers.** (**A** and **B**) Typical snapshots of D2 and D3 dimers under fs-laser pulses (repetition rate 1 kHz, fluence 2.4 mJ/cm$^2$) illumination at different times (see also Movies S4 and S5). The red-blue arrows show the orientations of the dimer at different times, and the pink arc arrows indicate the rotation directions. (**C** and **D**) Trajectories of the center of mass of D2 (from 0 to 52 s) and D3 dimer (from 0 to 68 s). Scale bars in the insets are 100 nm.

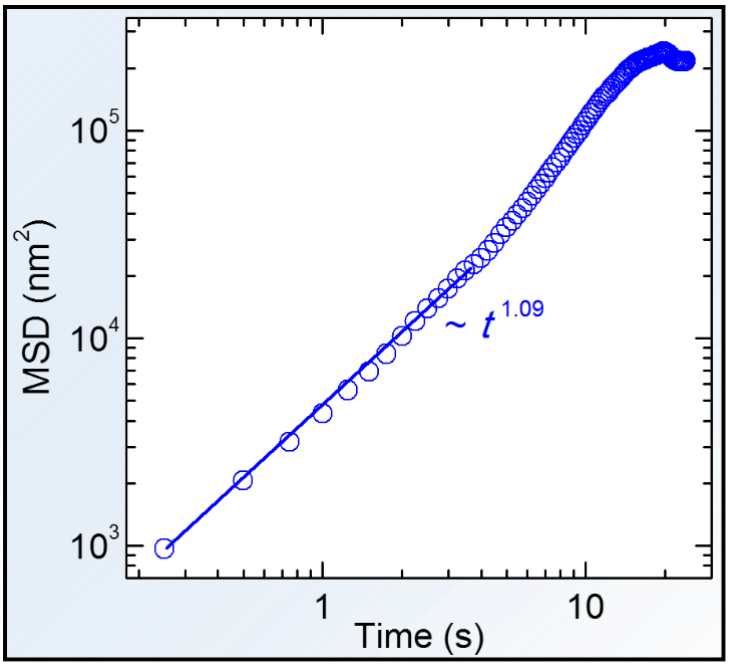


**Fig. S9. Translational MSD of D1 dimer as a function of time.** In the time range up to 10 s, the measured MSD linearly increases with time in the log-log plot with a slope of ~1.09, i.e. $MSD \propto N^{1.09}$, which exhibits approximately normal diffusion behavior with the diffusion coefficient of ~$1.1\times10^3$ nm$^2$/s. This diffusion coefficient is four orders of magnitude greater than that of the gold NPs without laser excitation (*22*).

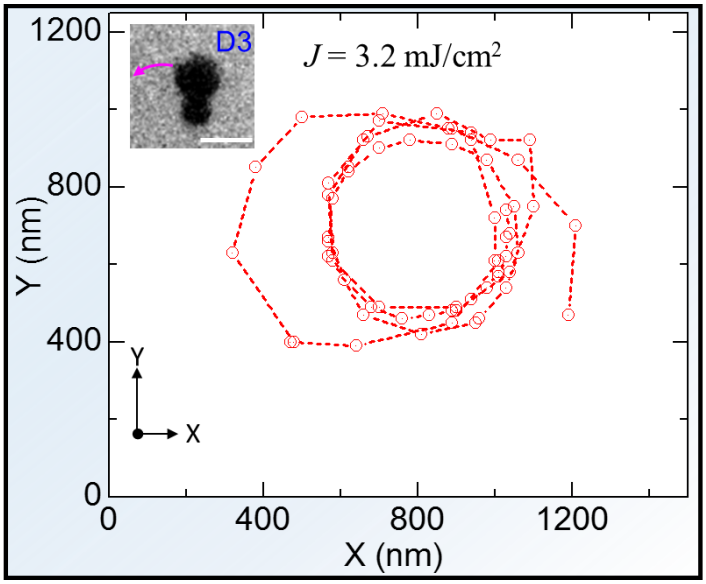


**Fig. S10. Trajectory of the center of mass of the highly asymmetric D3 dimer under a higher laser fluence of 3.2 mJ/cm$^2$ (from 0 to 65 s). Scale bar is 100 nm.**

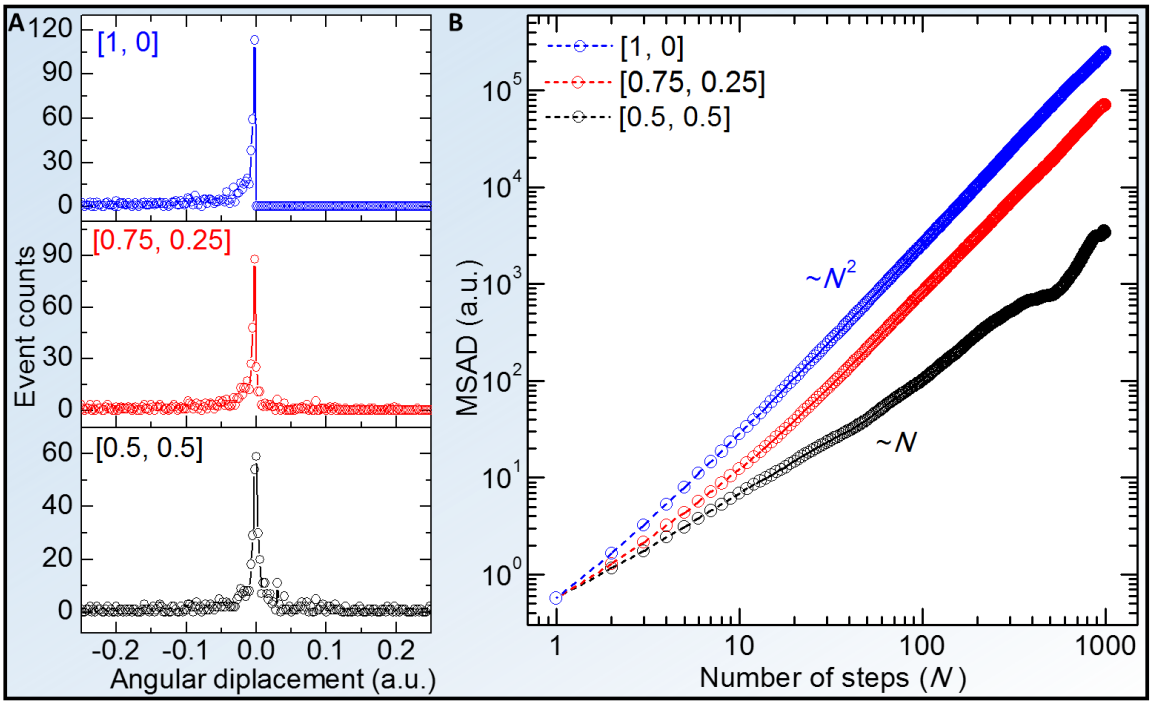


**Fig. S11. Theoretical simulations of random rotation with different biased angular displacement distributions.** (**A**) The angular displacement distributions of three types of random rotation with different biased angular displacement distributions of [0.5,0.5], [0.75, 0.25] and [1, 0], respectively (see Supplementary Text). (**B**) The MSADs of these three kinds of random rotations as a function of steps number $N$ (corresponding to the time $t$ in the experiment), respectively.

**Movie S1**

Rotation of a gold NP-dimer induced by a chain of fs-laser pulses excitation (fluence 4.5 $mJ/cm^2$, repetition rate 1 kHz).

**Movie S2**

Rotation of a gold NP-cluster induced by a single fs-laser pulse excitation (fluence 20 $mJ/cm^2$).

**Movie S3**

Rotation of D1 dimer induced by 1 kHz fs-laser pulses excitation with a fluence of 2.4 $mJ/cm^2$.

**Movie S4**

Rotation of D2 dimer induced by 1 kHz fs-laser pulses excitation with a fluence of 2.4 $mJ/cm^2$.

**Movie S5**

Rotation of D3 dimer induced by 1 kHz fs-laser pulses excitation with a fluence of 2.4 $mJ/cm^2$.

**References and Notes**


1. I. M. Abrams, J. W. McBain, A closed cell for electron microscopy. *J. Appl. Phys.* **15**, 607–609 (1944). doi:10.1063/1.1707475 Medline

2. N. de Jonge, F. M. Ross, Electron microscopy of specimens in liquid. *Nat. Nanotechnol.* **6**, 695–704 (2011). doi:10.1038/nnano.2011.161 Medline

3. F. M. Ross, Opportunities and challenges in liquid cell electron microscopy. *Science* **350**, aaa9886 (2015). doi:10.1126/science.aaa9886 Medline

4. M. J. Williamson, R. M. Tromp, P. M. Vereecken, R. Hull, F. M. Ross, Dynamic microscopy of nanoscale cluster growth at the solid-liquid interface. *Nat. Mater.* **2**, 532–536 (2003). doi:10.1038/nmat944 Medline

5. J. M. Yuk, J. Park, P. Ercius, K. Kim, D. J. Hellebusch, M. F. Crommie, J. Y. Lee, A. Zettl, A. P. Alivisatos, High-resolution EM of colloidal nanocrystal growth using graphene liquid cells. *Science* **336**, 61–64 (2012). doi:10.1126/science.1217654 Medline

6. H. Zheng, R. K. Smith, Y. W. Jun, C. Kisielowski, U. Dahmen, A. P. Alivisatos, Observation of single colloidal platinum nanocrystal growth trajectories. *Science* **324**, 1309–1312 (2009). doi:10.1126/science.1172104 Medline

7. H.-G. Liao, L. Cui, S. Whitelam, H. Zheng, Real-time imaging of Pt3Fe nanorod growth in solution. *Science* **336**, 1011–1014 (2012). doi:10.1126/science.1219185 Medline

8. E. Sutter, K. Jungjohann, S. Bliznakov, A. Courty, E. Maisonhaute, S. Tenney, P. Sutter, In situ liquid-cell electron microscopy of silver-palladium galvanic replacement reactions on silver nanoparticles. *Nat. Commun.* **5**, 4946 (2014). doi:10.1038/ncomms5946 Medline

9. Z. Zeng, W.-I. Liang, H.-G. Liao, H. L. Xin, Y.-H. Chu, H. Zheng, Visualization of electrode-electrolyte interfaces in $LiPF_6$/EC/DEC electrolyte for lithium ion batteries via in situ TEM. *Nano Lett.* **14**, 1745–1750 (2014). doi:10.1021/nl403922u Medline

10. S. Thiberge, A. Nechushtan, D. Sprinzak, O. Gileadi, V. Behar, O. Zik, Y. Chowers, S. Michaeli, J. Schlessinger, E. Moses, Scanning electron microscopy of cells and tissues under fully hydrated conditions. *Proc. Natl. Acad. Sci. U.S.A.* **101**, 3346–3351 (2004). doi:10.1073/pnas.0400088101 Medline

11. D. B. Peckys, N. de Jonge, Visualizing gold nanoparticle uptake in live cells with liquid scanning transmission electron microscopy. *Nano Lett.* **11**, 1733–1738 (2011). doi:10.1021/nl200285r Medline

12. N. de Jonge, D. B. Peckys, G. J. Kremers, D. W. Piston, Electron microscopy of whole cells in liquid with nanometer resolution. *Proc. Natl. Acad. Sci. U.S.A.* **106**, 2159–2164 (2009). doi:10.1073/pnas.0809567106 Medline

13. J. Park, H. Elmlund, P. Ercius, J. M. Yuk, D. T. Limmer, Q. Chen, K. Kim, S. H. Han, D. A. Weitz, A. Zettl, A. P. Alivisatos, 3D structure of individual nanocrystals in solution by electron microscopy. *Science* **349**, 290–295 (2015). doi:10.1126/science.aab1343 Medline

14. B. Barwick, H. S. Park, O.-H. Kwon, J. S. Baskin, A. H. Zewail, 4D imaging of transient structures and morphologies in ultrafast electron microscopy. *Science* **322**, 1227–1231 (2008). doi:10.1126/science.1164000 Medline

15. A. Yurtsever, A. H. Zewail, 4D nanoscale diffraction observed by convergent-beam ultrafast electron microscopy. *Science* **326**, 708–712 (2009). doi:10.1126/science.1179314 Medline

16. O.-H. Kwon, A. H. Zewail, 4D electron tomography. *Science* **328**, 1668–1673 (2010). doi:10.1126/science.1190470 Medline

17. A. H. Zewail, Four-dimensional electron microscopy. *Science* **328**, 187–193 (2010). doi:10.1126/science.1166135 Medline

18. U. J. Lorenz, A. H. Zewail, Observing liquid flow in nanotubes by 4D electron microscopy. *Science* **344**, 1496–1500 (2014). doi:10.1126/science.1253618 Medline

19. M. T. Hassan, H. Liu, J. S. Baskin, A. H. Zewail, Photon gating in four-dimensional ultrafast electron microscopy. *Proc. Natl. Acad. Sci. U.S.A.* **112**, 12944–12949 (2015). doi:10.1073/pnas.1517942112 Medline

20. Materials and methods are available as supplementary materials.

21. T. Li, S. Kheifets, D. Medellin, M. G. Raizen, Measurement of the instantaneous velocity of a Brownian particle. *Science* **328**, 1673–1675 (2010). doi:10.1126/science.1189403 Medline

22. H. Zheng, S. A. Claridge, A. M. Minor, A. P. Alivisatos, U. Dahmen, Nanocrystal diffusion in a liquid thin film observed by in situ transmission electron microscopy. *Nano Lett.* **9**, 2460–2465 (2009). doi:10.1021/nl9012369 Medline

23. C. Sönnichsen, A. P. Alivisatos, Gold nanorods as novel nonbleaching plasmon-based orientation sensors for polarized single-particle microscopy. *Nano Lett.* **5**, 301–304 (2005). doi:10.1021/nl048089k Medline

24. G. Roosen, C. Imbert, The TEM*$_{01}$ mode laser beam—A powerful tool for optical levitation of various types of spheres. *Opt. Commun.* **26**, 432–436 (1978). doi:10.1016/0030-4018(78)90240-7

25. X. Xu, C. Cheng, Y. Zhang, H. Lei, B. Li, Scattering and extinction torques: How plasmon resonances affect the orientation behavior of a nanorod in linearly polarized light. *J. Phys. Chem. Lett.* **7**, 314–319 (2016). doi:10.1021/acs.jpclett.5b02375 Medline

26. S. Link, C. Burda, B. Nikoobakht, M. El-Sayed, How long does it take to melt a gold nanorod?: A femtosecond pump–probe absorption spectroscopic study. *Chem. Phys. Lett.* **315**, 12–18 (1999). doi:10.1016/S0009-2614(99)01214-2

27. R. Lachaine, E. Boulais, M. Meunier, From thermo- to plasma-mediated ultrafast laser-induced plasmonic nanobubbles. *ACS Photonics* **1**, 331–336 (2014). doi:10.1021/ph400018s

28. E. Lukianova-Hleb, Y. Hu, L. Latterini, L. Tarpani, S. Lee, R. A. Drezek, J. H. Hafner, D. O. Lapotko, Plasmonic nanobubbles as transient vapor nanobubbles generated around

plasmonic nanoparticles. *ACS Nano* **4**, 2109–2123 (2010). doi:10.1021/nn1000222 Medline

29. P. Langevin, Sur la théorie du mouvement brownien. *C. R. Acad. Sci. Paris* **146**, 530 (1908).
30. L. Hong, S. M. Anthony, S. Granick, Rotation in suspension of a rod-shaped colloid. *Langmuir* **22**, 7128–7131 (2006). doi:10.1021/la061169e Medline
31. D. Mukhija, M. J. Solomon, Translational and rotational dynamics of colloidal rods by direct visualization with confocal microscopy. *J. Colloid Interface Sci.* **314**, 98–106 (2007). doi:10.1016/j.jcis.2007.05.055 Medline
32. A. S. Bodrova, A. V. Chechkin, A. G. Cherstvy, H. Safdari, I. M. Sokolov, R. Metzler, Underdamped scaled Brownian motion: (non-)existence of the overdamped limit in anomalous diffusion. *Sci. Rep.* **6**, 30520 (2016). doi:10.1038/srep30520 Medline
33. S. Kheifets, A. Simha, K. Melin, T. Li, M. G. Raizen, Observation of Brownian motion in liquids at short times: Instantaneous velocity and memory loss. *Science* **343**, 1493–1496 (2014). doi:10.1126/science.1248091 Medline